frontiers | Frontiers in Earth Science

TYPE Original Research
PUBLISHED 11 January 2023
DOI 10.3389/feart.2022.1007902

OPEN ACCESS

EDITED BY
Hao Zou,
Chengdu University of Technology, China

REVIEWED BY
Mao Luo,
State Key Laboratory of Palaeobiology and Stratigraphy (CAS), China
Xiaoqun Yang,
Institute of Geology and Geophysics (CAS), China

*CORRESPONDENCE
Xun Kang,
kangxunk@163.com

SPECIALTY SECTION
This article was submitted to Economic Geology, a section of the journal Frontiers in Earth Science

RECEIVED 31 July 2022
ACCEPTED 30 September 2022
PUBLISHED 11 January 2023

CITATION
Xu D, Qu Y, Huang L, Dai C, Hu R and Kang X (2023), Authigenic calcite as a record of geologic fluids in siliciclastic rocks: Evidences from the Upper Permian Wuerhe Formation, Junggar basin, NW China.
Front. Earth Sci. 10:1007902.
doi: 10.3389/feart.2022.1007902

Authigenic calcite as a record of geologic fluids in siliciclastic rocks: Evidences from the Upper Permian Wuerhe Formation, Junggar basin, NW China

Duonian Xu[1], Yongqiang Qu[1], Linjun Huang[1], Chao Dai[2,3], Ruipu Hu[2,3] and Xun Kang[2,3]*

[1]Research Institute of Petroleum Exploration and Development Northwest Branch, Lanzhou, China, [2]School of Geosciences and Info-Physics, Central South University, Changsha, China, [3]Key Laboratory of Metallogenic Prediction of Nonferrous Metals and Geological Environment Monitoring, Ministry of Education, Central South University, Changsha, China

The identification of geologic fluids and related fluid–rock interactions during diagenesis is the subject of much research in sedimentary petrology. Authigenic calcite potentially provides a record of geologic fluids and it occurs heterogeneously in the Upper Permian Wuerhe Formation (P_3w) in the Shawan Sag, Junggar Basin, which has a complex history of geologic fluid activity. This provides an ideal opportunity to study the effectiveness of authigenic calcite in tracing fluids. We conducted optical, cathodoluminescence (CL), and scanning electron microscopic observations, as well as the major and trace element and stable carbon and oxygen isotopes of authigenic calcite. The results show that three generations of calcite were precipitated in the P_3w Formation, and the diagenetic fluid was affected to varying degrees by paleo-meteoric water and hydrocarbon-bearing fluids. During early diagenesis, diagenetic fluid with low Mn contents precipitated the amorphous early-stage calcite (dark red in CL images, MnO <1.5%, $\delta^{13}C$ = −8.6‰ to 2.1‰, VPDB). Its carbon source was mainly meteoric CO_2. During mesodiagenesis, the limited hydrocarbon emplacement during the Middle Jurassic enriched the pore fluids in Mn and ^{13}C-depleted organic derived CO_2, subsequently precipitating the late-stage sparry calcite I (orange in CL images with MnO of 2.5%–4% and $\delta^{13}C$ of −14.5‰ to −8.1‰). The carbon in this calcite came from the dissolution of early-stage calcite and CO_2 generated by decarboxylation of organic acids. During the Early Cretaceous, large-scale hydrocarbon charging occurred and the pore fluids were further enriched in Mn and organic derived CO_2, eventually precipitating the late-stage sparry calcite II (bright yellow in CL images with MnO of >4% and $\delta^{13}C$ of −25.7‰ to −14.9‰). Its carbon source was mainly CO_2 produced by the decarboxylation of organic acids. The precipitation of abundant late-stage ^{s}C-depleted calcite suggests that the hydrocarbons were oxidized to organic acids in the reservoir. The two periods of hydrocarbon charging caused the dissolution of laumontite and the early-stage calcite, forming secondary minerals and dissolution pores, which increased the porosity and permeability of the rock. Therefore, authigenic calcite is a useful tracer of

fluid properties, fluid–rock interactions, and alteration processes in petroliferous basins.

KEYWORDS

authigenic calcite, geologic fluids, fluid-rock interaction, Upper Permian Wuerhe Formation, Junggar basin

Introduction

Siliciclastic petroleum reservoirs are distributed widely in petroliferous basins worldwide. For example, in China, the measured petroleum resources hosted in siliciclastic rocks account for >70% of total petroleum resources (Li, 2004; Ma et al., 2017). In petroliferous basins, meteoric water, hydrocarbon-bearing fluids, deep mantle-sourced fluids, and other external fluids can alter the diagenetic pathways of siliciclastic rocks by triggering fluid–rock interactions or by forming or destroying reservoir space (Jin et al., 2002; Seewald, 2003; Xie et al., 2009; Yuan et al., 2017; Huang et al., 2021; Zhi et al., 2022). Identifying these fluids is necessary for better understanding diagenesis and alteration in siliciclastic reservoirs and improving the evaluation of these reservoirs.

Typical authigenic minerals, such as calcite, pyrite, and quartz, can potentially record geologic fluids in altered sedimentary rocks. The precipitation of different generations of authigenic minerals can be identified using crystal morphology, cathodoluminescence (CL) images, and the relationships between minerals. The fluids that form authigenic calcite can then be identified from the chemical and stable carbon and oxygen isotopic compositions of the calcite, and the corresponding fluid–rock interactions can be further deciphered (Irwin et al., 1977; Spiro, 1977; Krouse et al., 1988; Zhu et al., 2006; Drake et al., 2015; Hu et al., 2018). In carbonate rocks, major element (e.g., iron and manganese), trace element (e.g., uranium), and carbon and oxygen isotopic compositions have been combined to identify different stages of calcite formation, alongside the source of their carbon and their formation processes (Irwin et al., 1977; Zhao et al., 2016; Xie et al., 2020; Sun et al., 2021). Thermochemical sulfate reduction accompanied by hydrocarbon oxidation has been identified using the relationships between authigenic minerals, the geochemical characteristics of H_2S-enriched natural gas, ^{13}C-enriched residual hydrocarbons, and the negative $\delta^{13}C$ values of authigenic calcite (Krouse et al., 1988; Zhu et al., 2006; Hao et al., 2008; Liu et al., 2020). In siliciclastic rocks, the precipitation of authigenic calcite with high MnO contents and extremely negative $\delta^{13}C$ values [down to −70‰ VPDB (Vienna Pee Dee Belemnite)] indicates hydrocarbon oxidation induced by high-valence Mn or Fe oxides (Hu et al., 2018; Kang et al., 2021). Therefore, authigenic calcite may record information implying the origin of geologic fluids and fluid–rock interactions in siliciclastic reservoirs.

The upper Permian Wuerhe (P_3w) Formation in the Shawan Sag is a coarse siliciclastic sedimentary sequence composed of gray sandy conglomerates and brown mudstones. During diagenetic stage, as well as diagenetic fluids, the rocks also affected by leaching by an external geologic fluid (e.g., meteoric water) and by hydrocarbon emplacement (Yuan et al., 2017; Zhi et al., 2022). Authigenic calcite with varying geochemical compositions was observed in the P_3w cores. This formation provides a good opportunity for testing the potential of using authigenic calcite to trace geological fluids in siliciclastic rocks; therefore, we conducted petrological and mineralogical studies of the P_3w Formation and used the *in situ* major element, trace element, and carbon and oxygen isotopic compositions of calcite formed in different stages to reveal the possible composition of geologic fluids that were present and the fluid–rock interactions and alteration of the reservoir that occurred during diagenesis.

Geologic setting

The study area is in the Shawan Sag in the west of the Junggar Basin, northwestern China, adjacent to the Zhongguai Uplift to the north, the Hongche Fault Zone to the west, the Homatu Anticline to the south, and the Western P1 Sag and Mosuowan Uplift to the east (Figure 1A). Since the late Carboniferous, the study area has been affected by subduction, accretion, and closure of the Darbute and northern Tianshan oceans, and several wedge-shaped fault depressions were developed in the sag (Han et al., 2006; Tang et al., 2010; Tao et al., 2021). At the end of the early Permian, the emergence of the structural wedge in the transition zone between the Shawan Sag and the Chepaizi Uplift caused the topography to slope gently from west to east (Liang et al., 2018). During the late Permian–Triassic, the strata were uplifted, exposed, and denuded, forming an unconformity. During the Cretaceous–Paleogene, the whole basin experienced steady subsidence. Since the Neogene, the large-scale thrusting adjacent to the Tianshan Mountains in response to the Himalayan Orogeny caused the sag to slope gradually southward, forming its current tectonic arrangement (Zhang et al., 1999; Zhang et al., 2006).

The late Permian Upper Wuerhe Formation (P_3w) unconformably overlies the middle Permian Lower Wuerhe Formation (P_2w) and also unconformably underlies the Lower Triassic Baikouquan (T_1b) Formation. The P_3w Formation is 150–210 m thick (Figure 1B) and was deposited in a coarse-grained fan delta system (Zou et al., 2007; Du et al., 2019). The formation is composed of coarse-grained gray and brown conglomerate with interbedded reddish-brown mudstone. The overall formation represents a fining upward sequence, and the

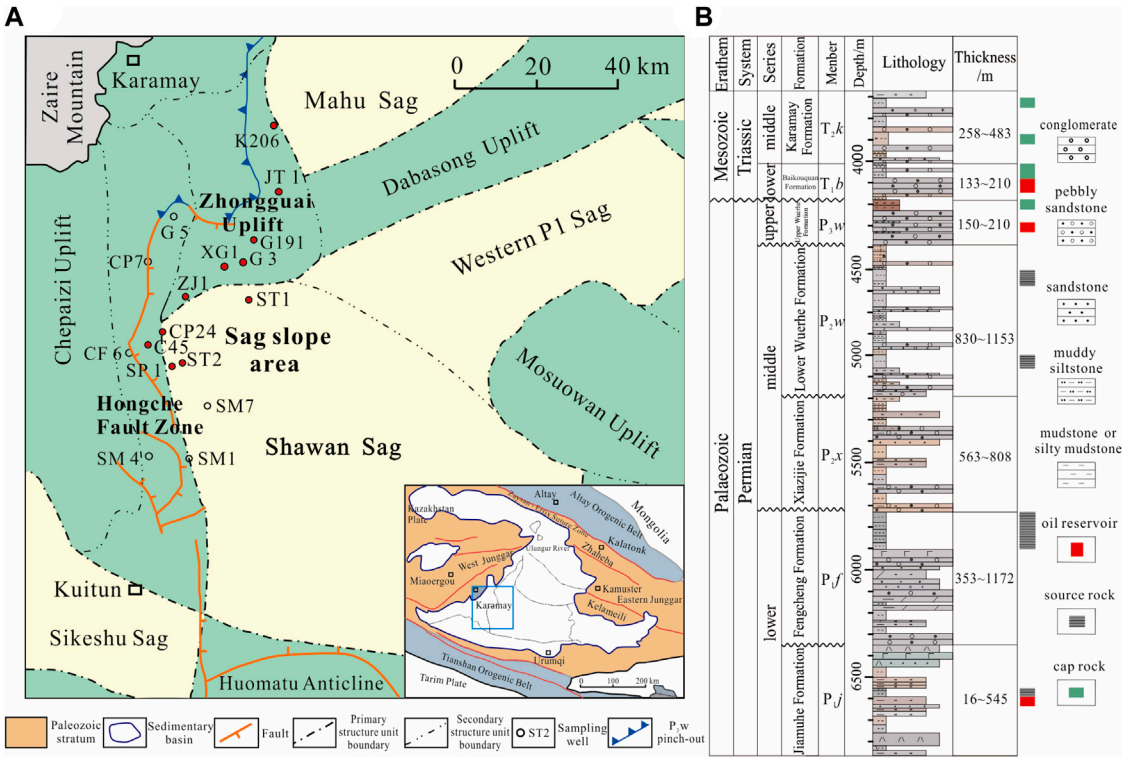

FIGURE 1
(A) Geologic map of the Shawan Sag and surrounding area. **(B)** Lithological column for the study area and typical geologic elements of the hydrocarbon reservoirs.

proportion of conglomerate decreases upward, reflecting a lake transgression systems tract.

Three mature to highly mature source rocks exist in the Shawan Sag—the Lower Wuerhe (P_2w), Fengcheng (P_1f), and Jiamuhe (P_1j) formations—leading to large-scale hydrocarbon production in the P_3w Formation (Zhang et al., 2015; Du et al., 2019; Xia et al., 2022). Two periods of oil and gas emplacement occurred (during the Middle Jurassic and Early Cretaceous) as the faults became active allowing migration (Wang, 2016; Pan et al., 2021). Since 2018, successful exploration has been carried out in the sandy conglomerate reservoir in the P_3w Formation. Daily oil and gas production from wildcat well ST1 reached 30.25 m^3 and 2.14 × 10^3 m^3, respectively, after hydraulic fracturing. High industrial oil and gas yields have also been obtained from well ST2, indicating that the reservoir shows a good prospect for future exploration and development (Kuang and Zhi, 2022).

TABLE 1 Core samples from the P_3w Formation.

well	samples	depth	Production test result
K206	6	3627.9–3642.5 m	Water layer
JT1	6	4453.5–4484.5 m	Water layer
	13	4502.5–4538.1 m	Water layer
CP24	6	4604.9–4610.8 m	Water layer containing oil
ST1	6	5281.9–5284.5 m	Water layer containing oil
	5	5309.3–5311.3 m	Water layer containing oil
G191	12	4333.2–4350.7 m	Heavy oil layer
ST2	8	4897.5–5168.6 m	Low-quality oil layer
	1	5171.0m	Dry layer
SP1	3	4828.5–4832.0 m	Dry layer
C45	7	4074.5–4220.3 m	Dry layer
XG1	3	4490.2–4491.9 m	Dry layer
G3	7	4610.5–4760.8 m	Gas layer
	6	4862.1–5260.5 m	Water layer

Sample descriptions and methods

Detailed core logging was conducted on 10 wells in the study area, and 89 core samples were collected systematically with vertical intervals of <1 m. Thin sections were studied under an optical microscope (Table 1). Thirty-two representative samples were analyzed using a scanning

electron microscope (SEM), and selected minerals were analyzed using energy dispersive spectroscopy (EDS). The SEM analyses were carried out on a TESCAN MIRA three using an accelerating voltage of 5 kV, 30 μm standard grating, and a counting time of 40 s, and the EDS analyses were carried out using an Oxford AZtec X-Max 150 detector with an accelerating voltage of 15 kV.

The different generations of authigenic calcite were identified using CL images, and the major element compositions of laumontite and each generation of calcite were measured using a JEOL JXA-8800 electron probe microanalyzer (EPMA). In addition, laser ablation–inductively coupled plasma–mass spectrometry (LA–ICP–MS) was used to analyze the trace element contents of authigenic calcite. We used a Jena PlasmaQuant MS Elite mass spectrometer with He as the carrier gas, a laser spot diameter of 40 μm, and an energy intensity of 3.5 J cm^{-2}. NIST SRM 610 was used as the external standard, and the Ca content obtained using the EPMA was used as the internal standard. The accuracy of the trace element analyses was <10%. Rare Earth element (REE) data were normalized to the composition of post-Archean Australian shale (PAAS) values.

The carbon and oxygen isotopic compositions of authigenic calcite from 29 samples were analyzed. Each sample aliquot of ca. 100–120 mg of rock powder (200 mesh) was cleaned in acetone for 2 h under ultrasound to remove adsorbed organic contaminants. After rinsing with deionized water, the aliquot was dried at 60°C. Half the aliquot was dissolved in a phosphate solution in a GasBench II system. The purified CO_2 gas was transferred to a Thermo Scientific MAT 253 isotope ratio mass spectrometer for analysis. The results were expressed relative to the VPDB standard using the Chinese standard GBW04416 ($\delta^{13}C$ = −6.06‰, $\delta^{18}O$ = −11.59‰) and expressed using δ notation. The accuracy of the C and O isotopic compositions is <0.10‰ and <0.08‰ (1 standard error), respectively.

To ascertain whether the crude oil in the study area has undergone microbial degradation, the composition of saturated hydrocarbons and biomarkers in the crude oil samples were also analyzed using a Shimadzu GC-2014 gas chromatograph and Shimadzu GCMS-QP2020 NX gas chromatography mass spectrometer, respectively.

Results

Petrology

The P_3w Formation contains mainly light gray and brown sandy conglomerate with interbedded brown mudstone. The clasts in the sandy conglomerate are dominated by lithic fragments (>90%; Figure 2A), with <10% quartz and feldspar grains (Figures 2C,D). The lithic fragments comprise mainly mafic–intermediate volcanic rock (Figure 2A), with low (<15%) metamorphic and sedimentary rock contents. The volcanic lithic fragments comprise mainly tuff (Figures 2A,B) with a small amount of basalt and andesite (Figure 2C). Poor sorting and subangular–subrounded clasts (Figure 2A) in the conglomerate demonstrate the low textural maturity of this formation and suggest that it was deposited close to provenance areas.

The reservoir rocks can be divided into oil-, gas-, and water-bearing and dry layers according to the fluid they host. Authigenic laumontite and calcite occur in oil-bearing layers alongside authigenic quartz and kaolinite (Figure 3B, D, E). Mixed-layer illite/smectite was observed in the intergranular pores (Figure 3C). Solid bitumen was also found in residual and secondary pores, indicating hydrocarbon emplacement (Figure 2E). Sparry laumontite and calcite with rare analcime are precipitated in the water-bearing layers (Figures 2C, 3F). Lithic clast surfaces are often coated with a mixed-layer illite/smectite. Dry layers have lower laumontite and calcite contents, and abundant mixed-layer illite/smectite coats the lithic grains and comprises the matrix in intergranular pores.

Diagenesis

During diagenesis, the P_3w Formation experienced mechanical compaction, mineral dissolution, cementation, and mineral replacement. Different diagenetic processes occurred in the different layers, particularly cementation and mineral dissolution. Because the studied strata have generally been buried to depths >4,000 m, all of the sandy conglomerates have undergone strong mechanical compaction. The grains have linear to concave and convex contacts (Figure 2A) and primary pores have been almost entirely destroyed (Figure 2B).

In the oil- and gas-bearing layers, laumontite and calcite occur as the primary cement (Figure 2F). Abundant secondary pores were generated by the extensive dissolution of laumontite and calcite cements and feldspar grains (Figures 2D,E, 3A). Bitumen often remains in the dissolution pores (Figure 2E). Late-stage calcite partially filled the pores formed by dissolution of laumontite and feldspar (Figure 2F, 4A, 5C). Authigenic quartz and vermicular kaolinite aggregates also occur in pores formed by dissolution of laumontite (Figures 3D,E). Leaf-like chlorite aggregates are often precipitated between grains (Figure 3C), and smectite has been gradually replaced by mixed-layer illite/smectite *via* illitization.

In the water-bearing layers, little dissolution has occurred and a small volume of dissolution porosity is found in only a few samples. Sparry laumontite and calcite form the primary cement (Figures 2B,C). Rare authigenic analcime occurs in several

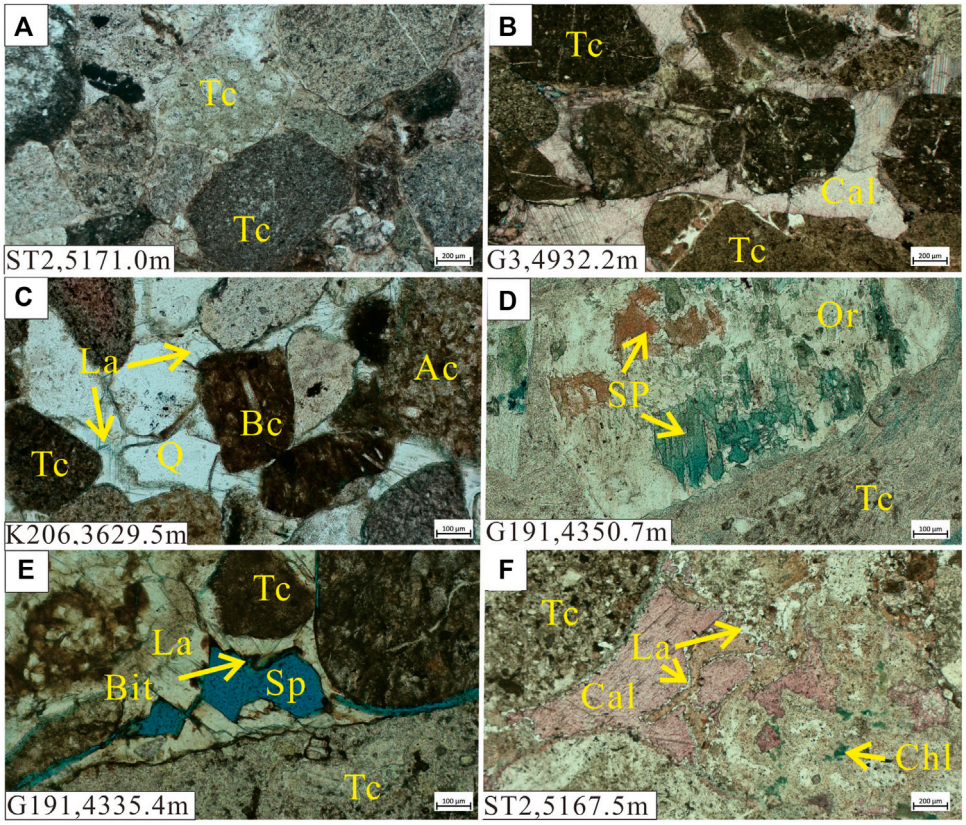

FIGURE 2
Photomicrographs of the Upper Wuerhe Formation. **(A)** Grayish white sandstone from a dry layer under plane-polarized light (PPL). **(B)** Water-bearing brown sandy conglomerate under PPL. **(C)** Water-bearing gray sandy conglomerate under PPL. **(D)** Brown gravelly conglomerate from a heavy oil-bearing layer under PPL. **(E)** Gray sandy conglomerate from a heavy oil-bearing layer under PPL. **(F)** Gray conglomerate from a low-quality oil-bearing layer under PPL. Tc: tuffaceous clast, Cal: calcite, Q: quartz, La: laumontite, Ac: andesite clast, Bc: basalt clast, Or: orthoclase, SP: secondary pores, Bit: bitumen, Chl: chlorite.

samples (Figure 3F). The dry layers have low zeolite and calcite contents and almost no dissolution has occurred. Smectite experienced extensive illitization, forming abundant mixed-layer illite/smectite (Figure 3C).

Calcite occurrence and geochemistry

In the oil-bearing layers, three generations of calcite can be identified by their dark red, orange, and bright yellow appearance in CL images (Figure 4). The dark red early-stage calcite occurs mainly as primary cement in primary pores and around the lithic grains (Figures 4C, 5A). The orange late-stage calcite I was precipitated mostly in primary pores through the recrystallization of early-stage calcite (Figure 4). The early-stage calcite in the oil- and gas-bearing layers has been partially dissolved then replaced by mixed-layer illite/smectite (Figure 5B). The bright yellow late-stage calcite II was precipitated in unconnected residual intergranular pores and pores formed by the dissolution of laumontite (Figures 4A, 5C,D). In the water-bearing layers, early-stage and late-stage calcite I commonly occurs with a small amount of late-stage calcite II in pores formed by the dissolution of laumontite (Figure 4A).

The authigenic calcite in the P_3w Formation has a wide range of MnO contents (Figure 6). Calcite in the oil-bearing layers yields MnO contents of 0.05%–5.06% (mean = 1.42%), the MnO contents of calcite in the water-bearing layers fall into two groups (0–1% and 2%–4%), and the MnO contents of calcite in the oil-bearing layers fall into three groups (<1.5%, 2.5%–4%, and 4%–6%; Figure 6). The FeO contents of calcite are generally <0.20%.

In situ LA–ICP–MS analyses were used to measure the REE contents of the calcite in the P_3w Formation and yielded light REE (LREE)/heavy REE (HREE) ratios of 2.20–7.80 (mean =

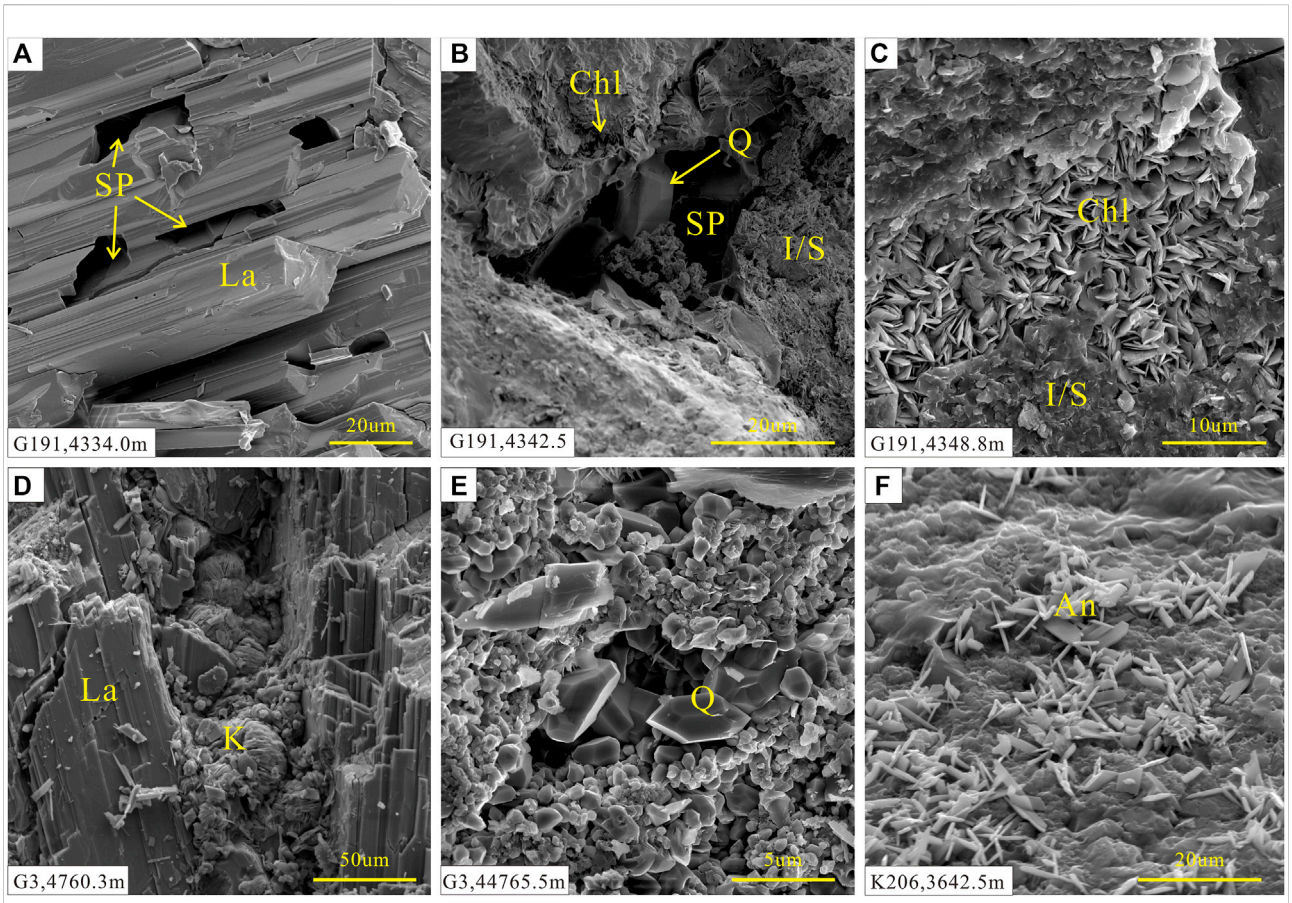

FIGURE 3
SEM images of intergranular minerals in the P_3w sandy conglomerates. **(A)** Gray sandy conglomerate from the heavy oil-bearing layer. **(B)** Gray sandstone from the heavy oil-bearing layer. **(C)** Gray–green sandy conglomerate from the heavy oil-bearing layer. **(D)** Gray sandy conglomerate from the gas-bearing layer. **(E)** Gray sandy conglomerate from the gas-bearing layer. **(F)** Gray gravelly conglomerate from the water-bearing layer. La: laumontite, SP: secondary pores, Chl: chlorite, Q: quartz, I/S: mixed-layer illite/smectite, **(K)** kaolinite, An: analcime.

5.17), showing LREE enrichment. The calcite yields Y/Ho ratios of 19.10–28.43 (mean = 21.77), negative Ce anomalies (δCe = 0.26–0.61; mean = 0.33), and positive Eu anomalies (δEu = 1.04–1.74; mean = 1.26).

Calcite carbon and oxygen isotopic compositions

The calcite in layers with different hydrocarbon charging intensities have different carbon isotopic compositions. The calcite in the oil-bearing layers is depleted in ^{13}C, with $\delta^{13}C$ values of −25.7‰ to −6.2‰ (mean = −14.1‰). The $\delta^{13}C$ values of calcite in the water-bearing layers is higher, at −12.4‰ to +1.2‰ (mean = −7.1‰). There are no clear differences in the oxygen isotopic compositions of the calcite among the different layers. The calcite in the oil-bearing layers yields $\delta^{18}O$ values of −20.9‰ to −13.6‰ (mean = −15.5‰), and the calcite in the water-bearing layers yields $\delta^{18}O$ values of −18.0‰ to −11.5‰ (mean = −15.6‰; Table 2).

Oil biomarkers

Previous studies have suggested that the crude oil hosted by the P_3w Formation may have been biodegraded near the fault zone (Pan et al., 2021); therefore, we analyzed crude oil biomarkers from the sampled layers. The total ion chromatogram from the crude oil from the study area shows a relatively complete sequence of *n*-alkanes, and typical biodegradation markers (e.g., 25-norhopanes) were not identified in the mass spectrum (Figure 7). Limited samples possibly underwent mild biodegradation as the existence of UCM (unidentified compound materials, Figure 7).

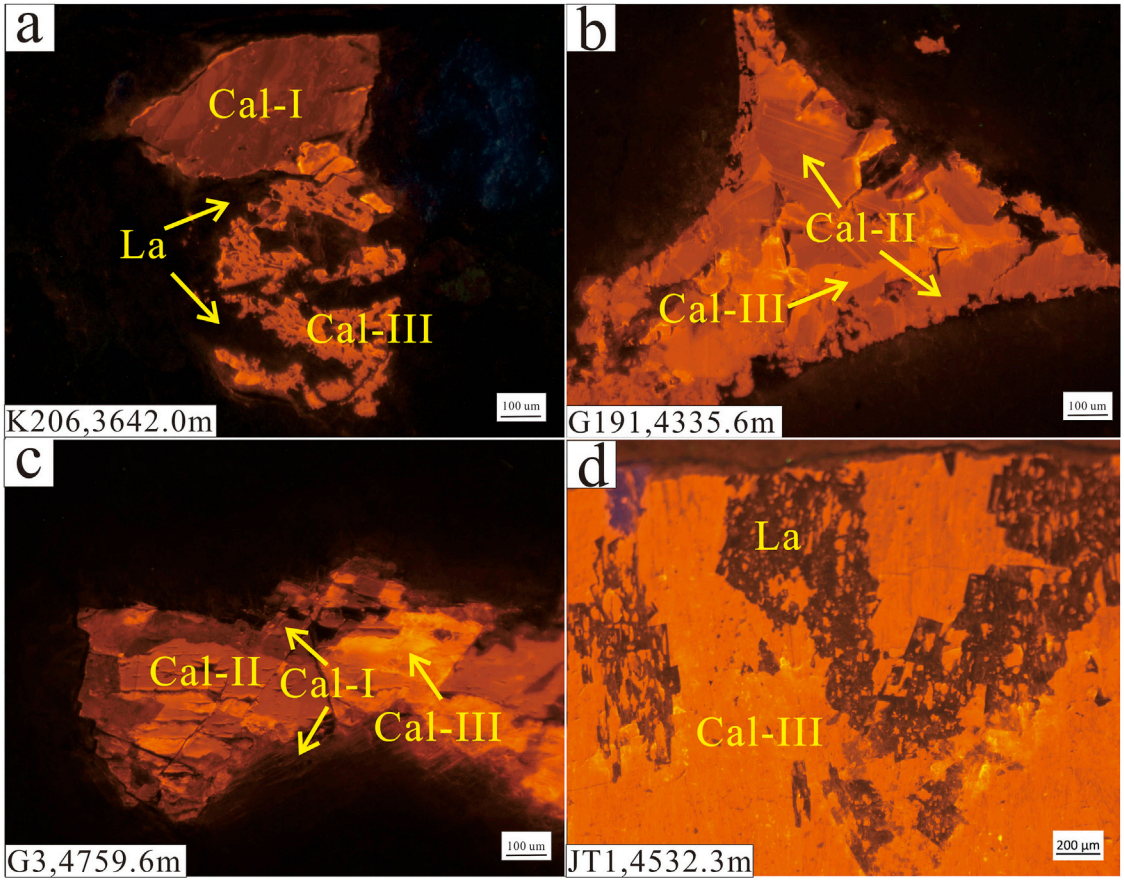

FIGURE 4
CL images of intergranular calcite cement in a sandy conglomerate from the P_3w Formation. **(A)** Gray fine-grained conglomerate from a water-bearing layer. **(B)** Gray sandy conglomerate from a heavy oil-bearing layer. **(C)** Gray conglomerate from a gas-bearing layer. **(D)** Gray sandstone from an oil-bearing layer. La: laumontite, Cal-I: early-stage calcite, Cal-II: late-stage calcite I, Cal-III: late-stage calcite II.

Discussion

Geologic fluid identification

The redox sensitive element (e.g., Mn and Fe) contents of calcite are closely related to the fluid from which it precipitated and can potentially indicate the geologic fluids present during diagenesis (Gregg and Shelton, 1989; Aggarwal et al., 2004; Liu et al., 2019). Previous studies have shown that hydrocarbon-bearing fluids in the Junggar Basin are enriched in Mn (Cao et al., 2007, 2020). In addition, in rocks containing red layers, the thermochemical oxidation of hydrocarbons by high-valence $Mn^{3+/4+}$ ions also releases Mn^{2+} ions into the pore water (Hu et al., 2018; Kang et al., 2021). Therefore, the MnO contents in calcite most likely reflect the intensity of hydrocarbon charging and subsequent hydrocarbon–water–rock interactions. Furthermore, the alteration of volcanic material may also lead to a slight increase in the Mn and Fe contents of pore water and a slight increase in its pH (Xi et al., 2015; Xie et al., 2020). In addition to elemental composition, the carbon isotopic compositions of calcite are also widely used to trace the sources of geological fluids, as calcite precipitated from meteoric water and calcite affected by ^{13}C-depleted organic carbon from hydrocarbons will have different carbon isotopic compositions (e.g., Irwin et al., 1977; Surdam et al., 1993; Seewald, 2003; Hu et al., 2018). The MnO contents in the three calcite stages and the lower $\delta^{13}C$ values of calcite in the hydrocarbon-bearing layers indicate that the diagenetic fluids were altered by hydrocarbon-bearing fluids during diagenesis (Irwin et al., 1977; Seewald, 2003; Cao et al., 2007; Zhi et al., 2022).

In the oil- and gas-bearing layers, some of the late-stage I calcite formed *via* recrystallization of early-stage calcite, and both of these generations of calcite are found mainly in the primary pores (Figures 4B,C). In contrast, the late-stage calcite II occurs mainly in secondary pores (Figure 5C), indicating that this calcite was precipitated after large-scale dissolution. As the MnO increase due to the alteration of volcanic material is limited,

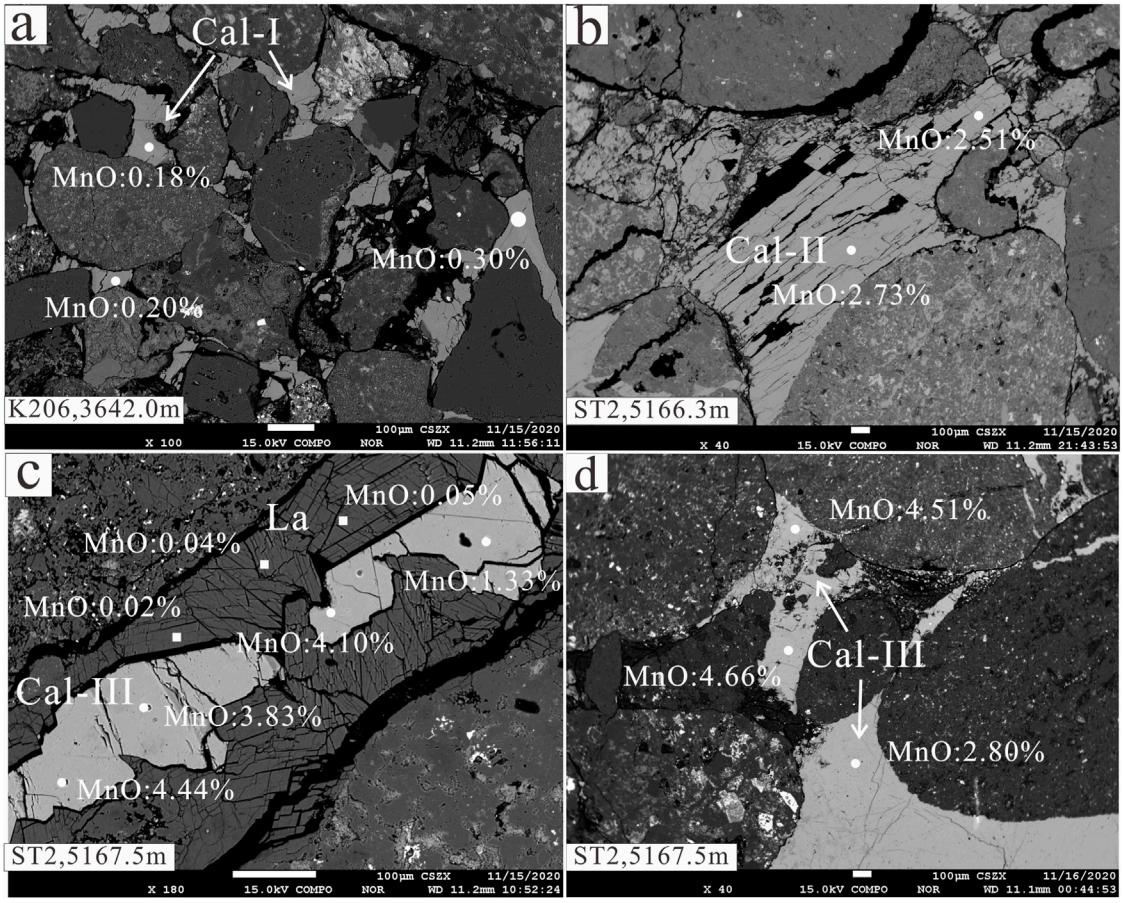

FIGURE 5
Backscattered electron images of laumontite and calcite in the P_3w Formation. **(A)** Gray sandstone from a water-bearing layer. **(B)** Gray sandy conglomerate from an oil-bearing layer. **(C)** Gray sandy conglomerate from an oil-bearing layer. **(D)** Gray sandy conglomerate from an oil-bearing layer. Cal-I: early-stage calcite, Cal-II: late-stage calcite I, Cal-III: late-stage calcite II, La: laumontite.

the higher MnO content of the late-stage calcite II reflects a change in the diagenetic fluid caused by hydrocarbon emplacement during diagenesis (Figure 6; Cao et al., 2007; Hu et al., 2018). The calcite in the oil- and gas-bearing layers yield a wide range of $\delta^{13}C$ values (−25.7‰ to −6.2‰), indicating that the source of the C in the calcite changed gradually during diagenesis from inorganic CO_2 in meteoric water to organic derived CO_2 from hydrocarbons (Irwin et al., 1977; Seewald, 2003). The early-stage calcite with low MnO contents (<1.5%) and high $\delta^{13}C$ and $\delta^{18}O$ values ($\delta^{13}C$ > −10.0‰; $\delta^{18}O$ > −15.0‰) was precipitated in the oil- and gas-bearing layers (Figures 6, 8), and the higher $\delta^{18}O$ values were inherited from meteoric water (Figure 8; Swart, 2015).

The first stage of hydrocarbon emplacement occurred during the Middle Jurassic (Wang, 2016; Pan et al., 2021); however little hydrocarbon charging occurred during this stage (Zhi et al., 2022). Organic acids and organic derived CO_2 in the hydrocarbon-bearing fluids led to a slight decrease in the pH and an increase in the Mn contents of the pore water (Cao et al., 2007; Hu et al., 2018) and provided organic carbon for the precipitation of the late-stage calcite (Seewald, 2003; Wu et al., 2017). This calcite generation is characterized by higher MnO contents (2.5%–4%) and slightly lower $\delta^{13}C$ values (−15.0‰ to −10.0‰). During the Early Cretaceous, a second, large-scale hydrocarbon charge further altered the diagenetic fluids, resulting in a series of hydrocarbon–water–rock interactions (Seewald, 2003; Swart, 2015; Kang et al., 2019; Sun et al., 2021). Organic acids and organic derived CO_2 dissolved in hydrocarbon-bearing fluids further reduced the pH of the pore water, and the decarboxylation of organic acids in moderately hot rocks also produced CO_2 (Irwin et al., 1977). Intense hydrocarbon charging led to further enrichment of the pore water in Mn and organic derived ^{13}C-depleted CO_2 (Cao et al., 2007; Zhi et al., 2022). Thermochemical oxidation of the hydrocarbons also likely occurred in some layers, forming organic acid intermediate, and even more ^{13}C-depleted CO_2 than

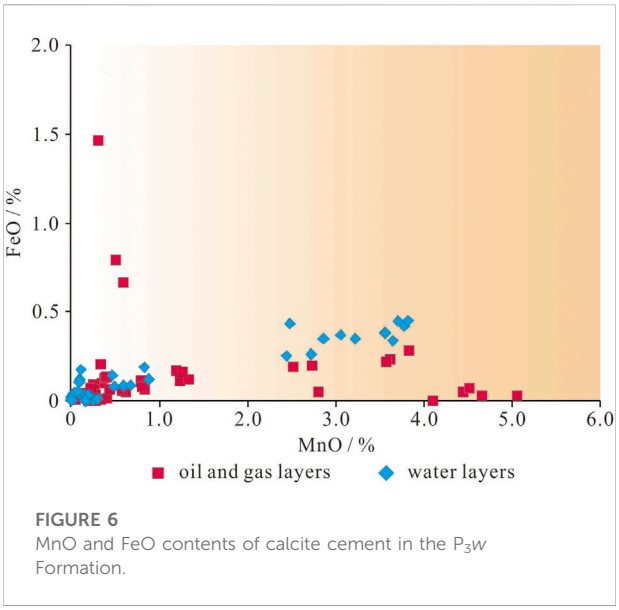

FIGURE 6
MnO and FeO contents of calcite cement in the P_3w Formation.

decarboxylation derived CO_2 (Seewald, 2003; Hu et al., 2018). The late-stage calcite that formed in this environment has high MnO contents (4%–6%) and low $\delta^{13}C$ values (less than −15.0‰; Figures 6, 8).

The water-bearing layers contain mainly early-stage and late-stage I calcite (Figure 5A), with a little late-stage II calcite precipitated in the pores formed during dissolution of laumontite (Figure 4A). The late-stage calcite in the water-bearing layers has low MnO contents (<1.0%; Figure 6), and their $\delta^{13}C$ values are generally lighter than −10.0‰ (Figure 8). This indicates that the diagenetic fluids in the water-bearing layers were not affected by large-scale hydrocarbon emplacement and inherited their compositions mainly from paleo-meteoric water (Zhi et al., 2022). However, in individual layers (e.g., at a depth of 3,629.5–3,642.0 m in well K206), the pore fluids might have been affected by water-soluble organic acids and CO_2 derived from hydrocarbons (Aggarwal et al., 2004; Minor et al., 2019). The late-stage calcite in these layers has high MnO contents (2.44%–3.82%) and negative $\delta^{13}C$ values (−12.4‰ to −10.7‰).

In the P_3w Formation, laumontite cement is abundant and widespread (Figure 2A) and is related to the alteration of volcanic lithic fragments in the rocks (Hay, 1966; Zhu et al., 2012). Laumontite can be observed in the water-, oil-, and gas-bearing layers (Figures 2C,E), indicating that the alteration of volcanic material was widespread. The moderately high MnO and FeO contents of early-stage calcite show that Mn^{2+} and Fe^{2+} ions were released into the pore water from the volcanic material during eodiagenesis, and the process slightly increased the pH of the pore water and promoted the precipitation of the early-stage calcite (Figure 6; Gieskes and Lawrence, 1981; Elderfield and Gieskes, 1982; Zhu et al., 2012).

Overall, the presence of calcite with low MnO contents (<1.5%) and moderately high $\delta^{13}C$ values (greater than −10.0‰) shows that the early diagenetic fluids in the study area were affected by meteoric water (Irwin et al., 1977; Aggarwal et al., 2004). The wide range of MnO contents (2.5%–6%) and lower $\delta^{13}C$ values (less than −10.0‰) of the authigenic calcite in the hydrocarbon-bearing layers indicate that during subsequent hydrocarbon charging the diagenetic fluid was altered by hydrocarbon-bearing fluids (Figures 6, 8). Individual water-bearing layers were also affected by water-soluble carboxylic acids and organic-matter derived CO_2. Moreover, in siliciclastic strata where oxidizing minerals occur, hydrocarbon–water–rock interactions promoted by high temperatures (>90°C) or microorganisms may cause hydrocarbon oxidation and generate organic acids and ^{13}C-depleted CO_2 (Surdam et al., 1993; Seewald, 2003; Hu et al., 2018; Wan et al., 2021). CO_2 generated *via* this process can lead to further precipitation of authigenic calcite with $\delta^{13}C$ values of less than −25‰ under alkaline conditions (Figure 8; Irwin et al., 1977; Hu et al., 2018).

Precipitation sequence of the authigenic minerals

Authigenic minerals are widespread in the P_3w Formation and characterized by multiple phases of precipitation (Figure 2). Multiple generations of authigenic minerals are products of changing geological fluids and complex fluid–rock interactions (Xie et al., 2020; Sun et al., 2021; Zhi et al., 2022). In the oil- and gas-bearing layers, hydrocarbon charging changed the diagenetic sequence, leading to the dissolution and re-precipitation of various secondary minerals (Walkden and Berry, 1984; Swart, 2015; Wu et al., 2017; Kang et al., 2019). During the early diagenetic stage, the pore water was transferred from the interbedded plastic mudstone layers to the clast-supported sandy conglomerate layers. As the burial depth increased, the temperature rose gradually, and the volcanic material experienced extensive alteration leading to the precipitation of authigenic laumontite as primary cement (Zhu et al., 2012). This process led to an increase in the pH of the pore water (Elderfield and Gieskes, 1982; Sample et al., 2017) and inorganic CO_2 and terrestrial Ca^{2+} concentrated gradually in the pore water, leading to precipitation of the early-stage calcite in residual intergranular pores (Figures 2B, 4C). There was a hiatus after the deposition of the P_3w Formation before the deposition of the overlying Early Triassic Baikouquan Formation, forming the Permian–Triassic unconformity around the sag (Figure 1B). This meant that the P_3w formation was affected by leaching by meteoric water during diagenesis (Yuan et al., 2017). The neutral to

TABLE 2 $\delta^{13}C$ and $\delta^{18}O$ values of calcite in the P_3w Formation.

Sample well	Depth, m	Lithology	Calcite stages	Well test result	$\delta^{13}C_{VPDB}$, ‰	$\delta^{18}O_{VPDB}$, ‰
K206-1	3627.9	Gray sandy conglomerate	Early- and Late-stage	Water layers	−8.3	−16.9
K206-2	3629.5		Early- and Late-stage		−10.7	−15.5
K206-3	3635.1	Gray inequigranular sandstone Gray sandy conglomerate	Early- and Late-stage		−8.6	−17.1
K206-4	3640.1		Early- and Late-stage		−12.4	−18.0
K206-5	3642.0		Early- and Late-stage		−10.9	−14.8
K206-6*	3642.5		Early-stage		−2.1	−11.5
PD1-8	5262.6	Gray muddy siltstone	Early-stage		−4.2	−16.2
JT1-7*	4482.8	Gray inequigranular sandstone	Early- and Late-stage		−7.3	−15.1
JT1-14*	4530.1	Gray granule conglomerate	Early-stage		1.2	−16.6
JT1-16*	4532.3	Gray mudstone	Early- and Late-stage		−6.8	−14.5
G3-9v	4932.2	Grayish brown Medium-fine conglomerate	Early- and Late-stage		−7.6	−15.8
G191-2	4334.0	Gray sandy granule conglomerate	Early- and Late-stage	Heavy oil layers	−14.9	−15.1
G191-5	4334.8		Early- and Late-stage		−13.7	−17.7
G191-6	4335.0		Early- and Late-stage		−8.8	−14.0
G191-7*	4335.2		Early- and Late-stage		−13.9	−14.4
G191-8*	4335.4	Gray muddy sandstone	Late-stage		−14.3	−16.6
G191-9	4335.5	Gray sandy granule conglomerate	Early- and Late-stage		−14.9	−20.9
G191-10	4335.6		Early- and Late-stage		−12.9	−19.3
G191-12	4350.7	Gary muddy siltstone	Late-stage		−25.7	−15.0
ST1-2*	5282.3	Grayish white sandy conglomerate	Early- and Late-stage	Oil layers containing water	−11.0	−13.8
ST1-3*	5282.9		Early- and Late-stage		−14.5	−14.7
ST1-6*	5284.5		Late-stage		−18.9	−16.3
ST1-10*	5310.9	Gray mudstone	Late-stage		−19.5	−15.0
ST2-4*	5165.7	Gray sandy conglomerate	Early- and Late-stage	Low-quality oil layers	−8.3	−14.6
ST2-5*	5166.3		Early- and Late-stage		−18.5	−15.4
ST2-6	5167.5		Early- and Late-stage		−19.9	−13.7
ST2-8	5168.6	Gray sandy granule conglomerate	Early- and Late-stage		−8.1	−13.6
G3-4	4641.9	Gray medium-fine conglomerate	Early- and Late-stage	Gas layers	−6.2	−14.2
G3-5	4759.6		Early- and Late-stage		−6.8	−14.7

*indicates the $\delta^{13}C$ and $\delta^{18}O$ data was cited from Zhi et al., 2022.

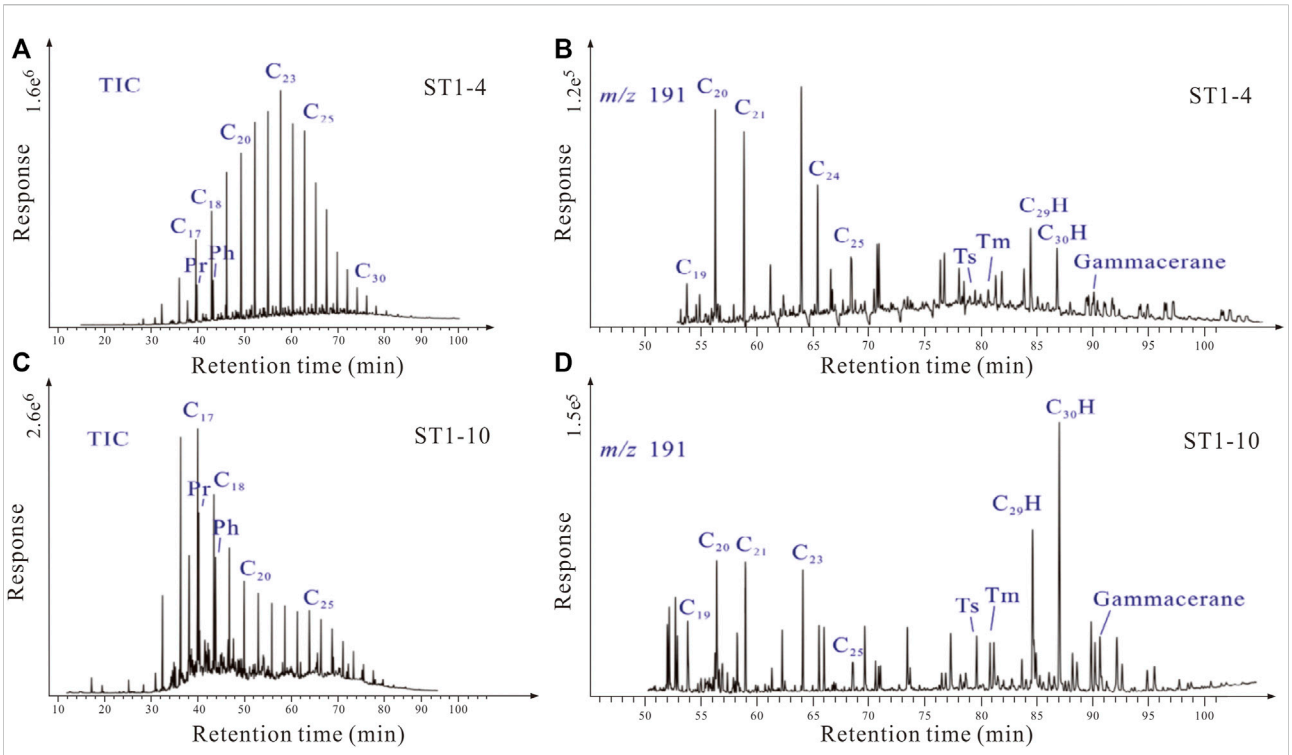

FIGURE 7
(A–C) Chromatograms and **(B–D)** mass spectrograms (with *m/z* ratio of 191) of crude oil samples from the P_3w Formation. Pr: pristane, Ph: phytane. **(A)** A complete sequence of *n*-alkanes in the total ion chromatogram (TIC) of ST1-4 oil sample. **(B–D)** 25-norhopanes were not found in *m/z* 191 mass spectrograms of ST1-4 and ST1-10 oil. **(C)** Limited unidentified compound materials occur in the total ion chromatogram of ST1-10 oil sample, indicating mild biodegradation.

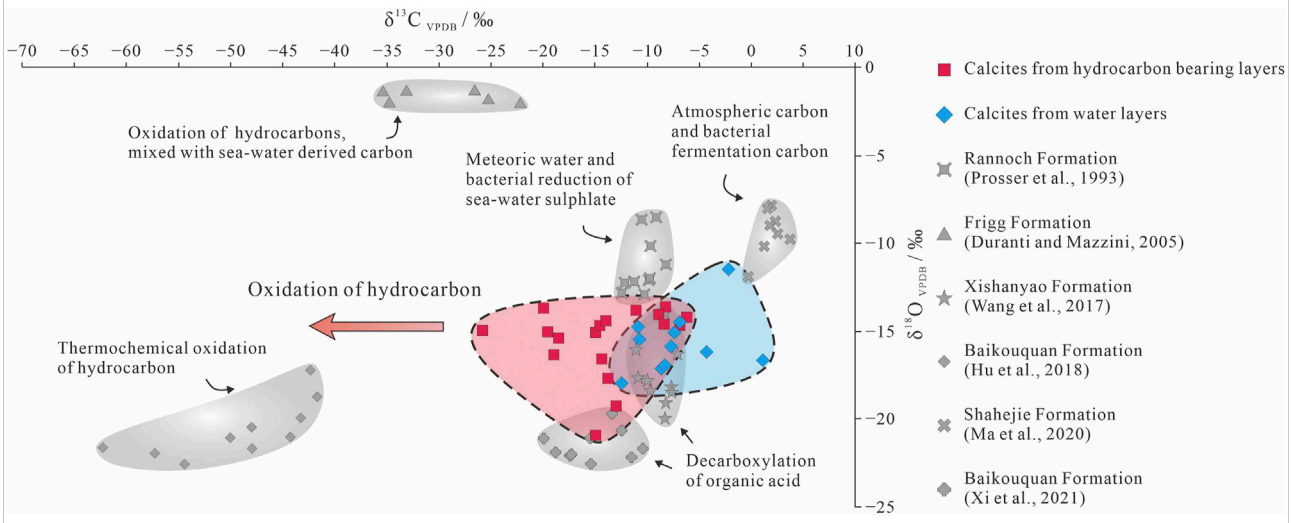

FIGURE 8
Carbon and oxygen isotopic compositions of the P_3w calcite compared with typical authigenic calcite in siliciclastic rocks.

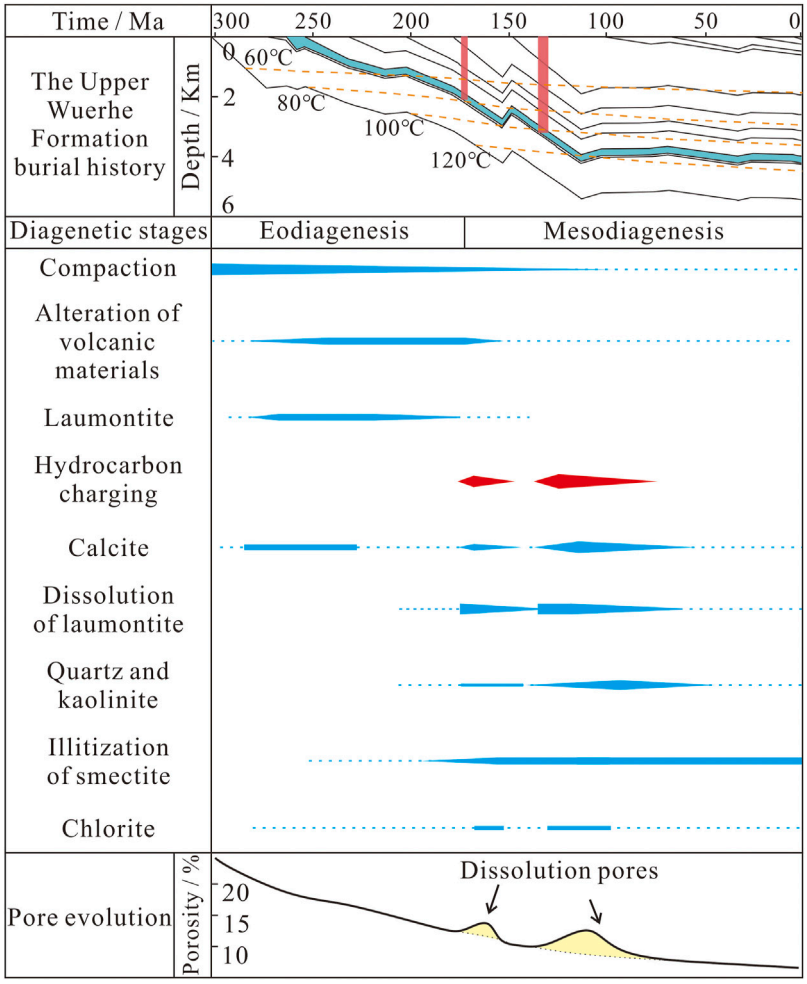

FIGURE 9
Integrated diagenetic evolution based on petrology and burial and thermal histories and their effect on the porosity of the P_3w sandy conglomerates. The burial history and thermal evolution of P_3w is taken from Well ZJ1. The stratigraphy is from Wang (2016), and the tectonic and geothermal evolution data are from Qiu et al. (2002).

acidic meteoric water changed the properties of the pore water and caused partial recrystallization of the early-stage calcite.

Limited hydrocarbon emplacement occurred during the Middle Jurassic (Figure 9; Pan et al., 2021). The acidic hydrocarbon-bearing fluids promoted the alteration of volcanic material and led to precipitation of the late-stage I calcite (Figure 5B). The second, large-scale hydrocarbon charging event during the Early Cretaceous introduced organic acids and organic derived CO_2 (Figure 9; Surdam et al., 1984, Surdam et al., 1989; Zhi et al., 2022), which further reduced the pH of the pore water, leading to extensive dissolution of laumontite and early-stage calcite (Figure 2E). These secondary pores became interconnected along cleavage fractures (Figure 3E) and retained small amounts of solid bitumen (Figure 2E). When the Ca^{2+}, Al^{3+}, and Si^{4+} ions released by the dissolution of laumontite and early-stage calcite reached saturation, secondary quartz and kaolinite precipitated in the pores (Figures 3D,E). Dissolution also buffered the pH of the pore water (Surdam et al., 1984, 1993), leading to the precipitation of late-stage calcite II in dissolution and residual intergranular pores (Figures 5C,D).

In the water-bearing and dry layers, alteration of volcanic lithic fragments and the pore water composition led to precipitation of laumontite and early-stage calcite during eodiagenesis. More sparry laumontite and calcite cements occur in the water-bearing layers than in the dry layers, as water aids ion transport (Figure 2C). Leaching by meteoric water also promoted recrystallization of early-stage calcite (Figures 2B, 5A). During mesodiagenesis, most minerals (including the laumontite cement) remained stable in the water-bearing layers, except for smectite, which was illitized.

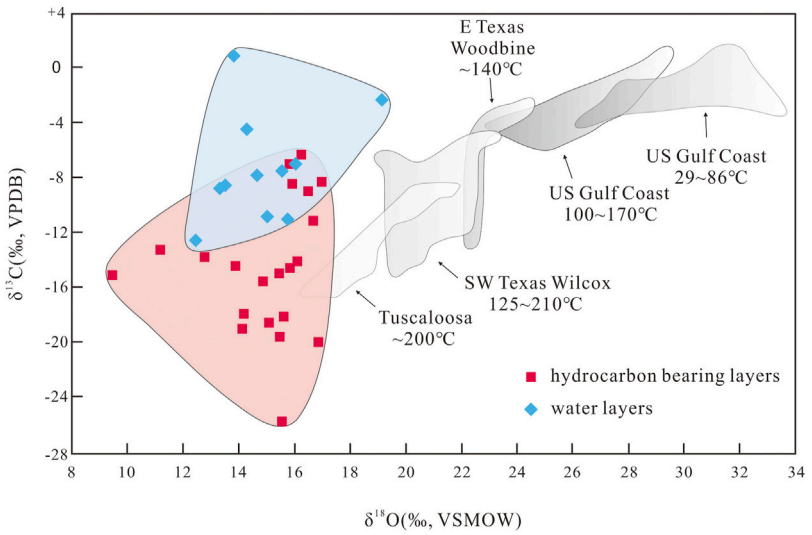

FIGURE 10
$\delta^{13}C$ and $\delta^{18}O$ values of calcite cement in the P_3w Formation compared with typical authigenic calcite in source rocks (modified from Franks and Forester, 1984).

Origin of organic acids in the reservoir

The late-stage calcite in the study area was affected by organic acids dissolved in the hydrocarbon-bearing fluids (Figure 8). A small amount of organic acid is dissolved in hydrocarbon-bearing fluids when they are extracted from source rocks (Irwin et al., 1977; Franks and Forester, 1984). The $\delta^{13}C$ values of the authigenic calcite in the oil- and gas-bearing layers of the P_3w Formation are lighter than those of calcite in typical source rocks (Figure 10), suggesting that insufficient organic acid was supplied from the source rocks to generate the ^{13}C-depleted late-stage calcite. Assuming that the maximum organic acid content in the in hydrocarbon-bearing fluids that migrated into the reservoirs in the P_3w Formation from the source rock was 10,000 mg L^{-1} (Shock, 1994), and that the porosity of the reservoir rock was 15% when the reservoir was charged by oil and gas, the organic acid in one cubic meter of rock could have generated 1,100 g of CO_2 through thermal decarboxylation. However, the calcite content of the formation is ~6%, which would have required 71,280 g of CO_2 per cubic meter of rock. As stable carbon isotopic fractionation is mass balanced, we can assume $\delta^{13}C$ values of −2‰ and −25‰ for the early-stage calcite and the calcite related to thermal decarboxylation of organic acids, respectively (Irwin et al., 1977; Hu et al., 2018). Using the carbon isotopic compositions of the calcite in the P_3w Formation, we can estimate that CO_2 from the thermal decarboxylation of organic acids accounts for 18%–100% (mean = 53%) of the calcite in the oil- and gas-bearing layers. In the water-bearing layers, this proportion reduces to 0%–45% (mean = 23%). Using these proportions, we still estimate that the authigenic calcite in one cubic meter of rock in the hydrocarbon- and water-bearing layers would have required 37,779 and 16,395 g, respectively, of CO_2 from the decarboxylation of organic acids. Both values are far higher than the 1,100 g supplied by the source rocks, which suggests that the supply of organic acids from source rocks was insufficient, and that additional organic acids were most likely produced in the reservoir rocks *via* interactions between organic hydrocarbons and inorganic minerals.

It has been suggested that hydrocarbons reacting with SO_4^{2-} or high-valance Fe and Mn oxides, induced by microorganisms or high temperatures, to generate organic acids after hydrocarbons are emplaced in a reservoir (Surdam et al., 1993; Seewald, 2003). The low $\delta^{13}C$ values (as low as −25.7‰) of the late-stage calcite confirm that hydrocarbon oxidation occurred in the P_3w reservoirs. The oxidation consisted of a series of intermediary reactions involving alkene, alcohol, ketone, and carboxylic acid, ultimately producing short-chained saturated hydrocarbons and CO_2 (Figure 11). The mineral oxidants provided a strong driving force for the reaction to proceed by consuming H_2 that would otherwise accumulate in pore fluids (Seewald, 2001). The rapid kinetics of the reactions that consume the alkene, alcohol, and ketone intermediaries resulted in very low concentrations of these species in solution during *n*-alkane oxidation, whereas the sluggish kinetics of the destruction of carboxylic acids by decarboxylation and oxidation would have allowed their certain concentrations in aqueous fluids (Seewald, 2001, 2003). The carboxylic acids most likely

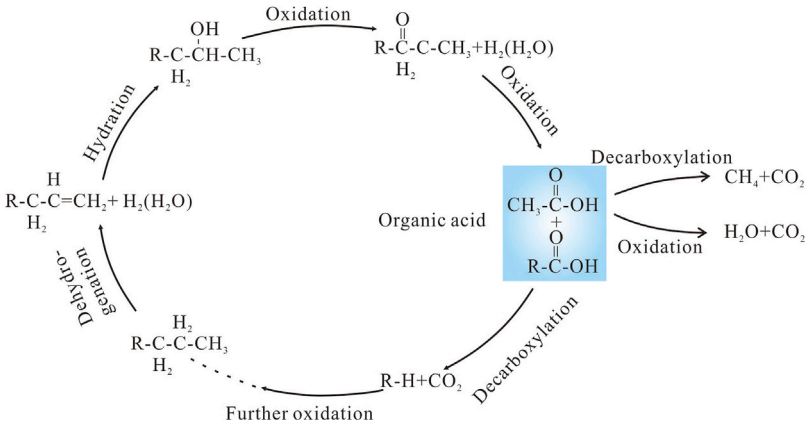

FIGURE 11
Reaction pathways for the oxidation of long-chain hydrocarbons alongside the reduction of high-valence Mn and Fe oxides. Modified after Seewald (2003).

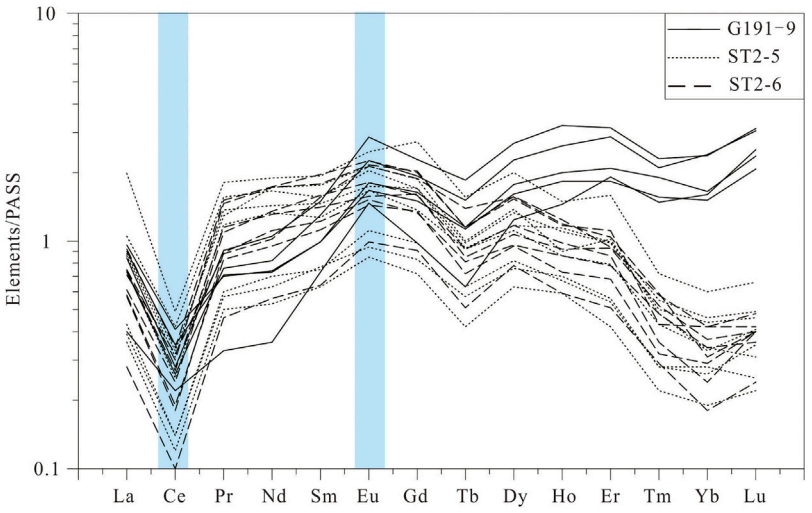

FIGURE 12
PAAS-normalized REE diagram for calcite in the P_3w Formation.

provided the excess organic derived CO_2 required to precipitate the calcite in the P_3w Formation.

The homogenization temperatures of fluid inclusions in the P_3w Formation indicate that they formed at temperatures of >80°C during hydrocarbon charging (Wang, 2016); such temperatures are not conducive to the metabolism and survival of bacteria (Peters et al., 2005). Moreover, the crude oil in the P_3w Formation contains a relatively complete n-alkane sequence, with no significant increase in typical microbial degradation biomarkers (e.g., 25-norhopanes; Figure 7), providing further evidence against the possibility that the organic acids were generated by microbial activity. In addition, no authigenic pyrite or H_2S were found in the samples, ruling out the possibility of thermochemical sulfate reduction (Krouse et al., 1988). Thus, some of the organic acids in the P_3w Formation were generated *via* the oxidation of hydrocarbons by high-valence Fe and Mn oxides at temperatures of >80°C.

The REE characteristics of the calcite also support an oxidized diagenetic environment during burial of the P_3w

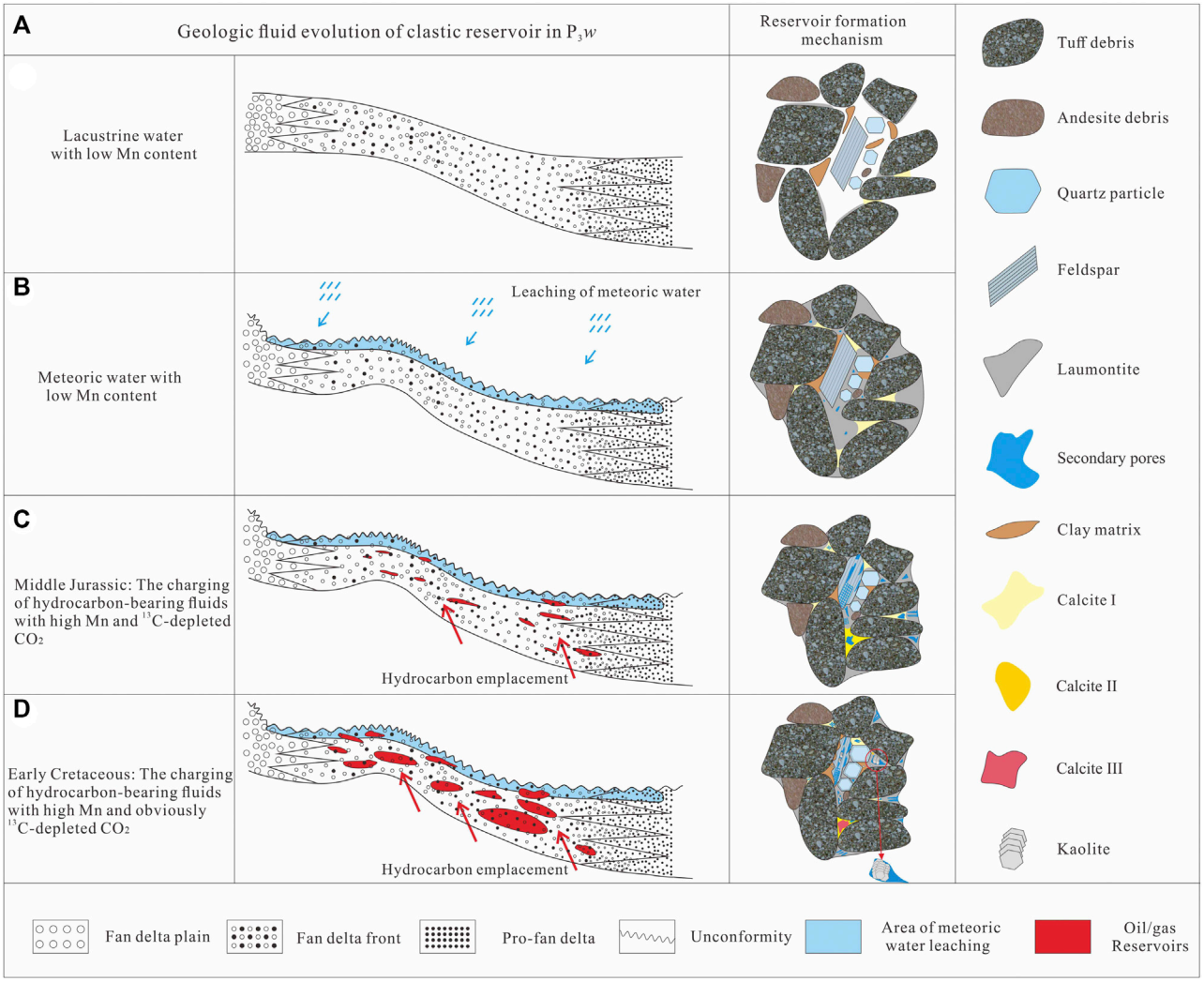

FIGURE 13
Evolution of the geologic fluid and formation of the P_3w reservoirs.

Formation. The calcite in this formation is enriched in LREEs relative to HREEs (Figure 12). Previous studies have shown that when crude oil or other organic matter is degraded, more LREEs than HREEs are released from hydrocarbon-bearing fluids into the pore water (Haley et al., 2004; Himmler et al., 2010). This process likely caused the LREE enrichment in the authigenic calcite. The calcite also yields negative Ce and positive Eu anomalies (Figure 12), indicating an oxidizing environment (Zhao, 1997). The calcite also yields high Y/Ho ratios (19.10–28.43). Bau and Dulski (1999) argued that Fe and Mn oxides and hydroxides preferentially adsorb Ho relative to Y in an oxidizing environment, thus increasing the Y/Ho ratios of diagenetic fluids. In addition, interbedded brown mudstone layers are found in the P_3w Formation, and hematite also exists in some conglomerate layers. These indicate an oxidizing diagenetic environment in this formation. It implies that organic acids were generated by the oxidation of long-chain hydrocarbons by oxidizing meterials when hydrocarbons migrated into reservoirs in the P_3w Formation.

Alteration of deeply buried siliciclastic reservoirs by fluid

Owing to the different volumes of meteoric water and hydrocarbon-bearing fluids, different fluid–rock interactions occurred in the hydrocarbon-bearing, water-bearing, and dry layers, which altered the diagenetic processes and affected reservoir quality. During the early stage of diagenesis, the P_3w Formation was only shallowly buried, leading to weak

compaction. Authigenic laumontite and early-stage calcite precipitated as primary cements, partially resisting compaction by the overlying strata (Figure 13A; Liu et al., 2019). As burial depth increased, increased compaction, the recrystallization of the early-stage calcite, and clay mineral precipitation reduced the residual primary porosity. During the depositional hiatus at the end of the Permian, the CO_2 supply from meteoric water caused slight dissolution of soluble components, including the laumontite cement and feldspar debris at the top of the formation, and these dissolution pores were filled mostly by recrystallized calcite. Thus, only limited secondary porosity formed close to the top of this formation owing to leaching by meteoric water (Figures 2, 13B).

During mesodiagenesis, a limited phase of hydrocarbon emplacement during the Middle Jurassic played an important role in alteration of the P_3w reservoirs. Owing to charging by acid hydrocarbon bearing fluids derived from the source rocks, the pH of the pore water in the reservoir decreased, preventing the precipitation of laumontite and calcite or promoting their dissolution and forming a small amount of secondary porosity. This period of hydrocarbon emplacement interrupted the decline in reservoir porosity caused by mechanical compaction, providing pore space for subsequent hydrocarbon accumulation and laying the foundation for further reservoir alteration (Figure 13C). After intense hydrocarbon charging during the Early Cretaceous, the high-temperature oxidation of hydrocarbons produced organic acids that added to those initially derived from the source rocks. The decrease in the pH of the pore fluids caused extensive dissolution of laumontite and early-stage calcite and produced abundant secondary pores. Overall, the two periods of hydrocarbon emplacement considerably increased the reservoir porosity and contributed to the formation of the P_3w reservoir beds (Figure 11D).

Conclusion

Multiple generations of calcite record the properties of and changes in diagenetic fluids and fluid–rock interactions in the P_3w Formation. In hydrocarbon-bearing layers, early diagenetic fluid mainly inherited its composition from paleo-meteoric water and precipitated early-stage calcite with low MnO contents (<1.5%) and normal $\delta^{13}C$ values (−10.0‰ to +2.0‰). During mesodiagenesis, limited hydrocarbon charging during the Middle Jurassic altered the diagenetic fluid, causing enrichment in Mn and ^{13}C-depleted organic derived CO_2, leading to precipitation of late-stage calcite I with high MnO contents (2.5%–4%) and negative $\delta^{13}C$ values (−10.0‰ to −15.0‰). Large-scale hydrocarbon emplacement during the Early Cretaceous produced diagenetic fluid that was more enriched in Mn and organic derived CO_2, thus forming late-stage calcite II, characterized by higher MnO contents (4%–6%) and more negative $\delta^{13}C$ values (less than −15.0‰). The emplacement of hydrocarbon-bearing fluids altered the diagenetic process substantially. The abundant volcanic lithic fragments in this formation were altered to form abundant authigenic laumontite during eodiagenesis, while hydrocarbon charging caused dissolution of laumontite and early-stage calcite and precipitation of other minerals, including kaolinite, quartz, and late-stage calcite. This process formed a network of dissolution pores, increasing the porosity and permeability of the rock. In contrast, in water-bearing and dry layers, most of the laumontite and calcite remained stable. In addition, in oxidizing rocks such as the P_3w formation, long-chain hydrocarbons can be oxidized to carboxylic acids that enhance diagenesis, as thermal decarboxylation forms ^{13}C-depleted CO_2. This study shows that authigenic calcite can record the properties of diagenetic fluids and the fluid–rock interactions that occur during diagenesis, and its composition can be used to identify diagenetic fluids in petroliferous basins.

Data availability statement

The raw data supporting the conclusions of this article will be made available by the authors, without undue reservation.

Author contributions

DX is the principal author and petrological interpreter, and also writes and edits the paper. YQ and LH contribute on the geological explanations, as well as writing/editing the paper. CD and RH conduct the geochemical analyses, and contribute on preparing the figures and writing the paper. XK provides the founding for this study and thoroughly edits the paper.

Funding

This work was financed by the National Natural Science Foundation of China (Grant Nos. 41902137), the China Hunan Provincial Science & Technology Department (2022WK 2004) and the Natural Science Foundation of Hunan Province (2020JJ5703). We extend our gratitude to Jeffery M. Dick for his helpful improving on the language.

Conflict of interest

The authors declare that the research was conducted in the absence of any commercial or financial relationships that could be construed as a potential conflict of interest.

Publisher's note

References

Aggarwal, P. K., Dillon, M. A., and Tanweer, A. (2004). Isotope fractionation at the soil-atmosphere interface and the ^{18}O budget of atmospheric oxygen. *Geophys. Res. Lett.* 31 (14), L14202. doi:10.1029/2004GL019945

Bau, M., and Dulski, P. (1999). Comparing yttrium and rare earths in hydrothermal fluids from the mid-atlantic ridge: implications for Y and REE behaviour during near-vent mixing and for the Y/Ho ratio of proterozoic seawater. *Chem. Geol.* 155 (1–2), 77–90. doi:10.1016/S0009-2541(98)00142-9

Cao, J., Hu, W. X., Yao, S. P., Zhang, Y. J., Wang, X. L., Zhang, Y. Q., et al. (2007). New inorganic geochemical indicators for tracing petroleum migration in Junggar Basin. *Sci. China Earth Sci.* 37 (10), 1358–1369. (in Chinese with English abstract). Available at: https://engine.scichina.com/doi/pdf/aeb4e4c0298d43348912d1e934726c32.

Cao, J., Xia, L., Wang, T., Zhi, D., Tang, Y., and Li, W. (2020). An alkaline lake in the late paleozoic ice age (lpia): A review and new insights into paleoenvironment and petroleum geology. *Earth. Sci. Rev.* 202 (2020), 103091. doi:10.1016/j.earscirev.2020.103091

Drake, H., Åström, M. E., Heim, C., Broman, C., Åström, J., Whitehouse, M., et al. (2015). Extreme ^{13}C depletion of carbonates formed during oxidation of biogenic methane in fractured granite. *Nat. Commun.* 6 (1), 7020–7029. doi:10.1038/ncomms8020

Du, J. H., Zhi, D. M., Tang, Y., Jia, C. M., and Xu, Y., (2019). Prospects in upper permian and strategic discovery in shawan sag, Junggar Basin. *China Pet. Explor* 24 (1), 24–35. doi:10.3969/j.issn.1672-7703.2019.01.004

Elderfield, H., and Gieskes, J. M. (1982). Sr isotopes in interstitial waters of marine sediments from Deep Sea Drilling Project cores. *Nature* 300 (5892), 493–497. doi:10.1038/300493a0

Franks, S. G., and Forester, R. W. (1984). Relationships among secondary porosity, pore-fluid chemistry and carbon dioxide, Texas gulf coast: Part 1. Concepts and principles. *AAPG Mem.* 37 (2), 63–80.

Gieskes, J. M., and Lawrence, J. R. (1981). Alteration of volcanic matter in deep sea sediments: Evidence from the chemical composition of interstitial waters from deep sea drilling cores. *Geochim. Cosmochim. Acta* 45 (10), 1687–1703. doi:10.1016/0016-7037(81)90004-1

Gregg, J. M., and Shelton, K. L. (1989). Minor-and trace-element distributions in the Bonneterre Dolomite (Cambrian), southeast Missouri: Evidence for possible multiple-basin fluid sources and pathways during lead-zinc mineralization. *Geol. Soc. Am. Bull.* 101 (2), 221–230. doi:10.1130/0016-7606(1989)101<0221:matedi>2.3.co;2

Haley, B. A., Klinkhammer, G. P., and McManus, J. (2004). Rare Earth elements in pore waters of marine sediments. *Geochim. Cosmochim. Acta* 68 (6), 1265–1279. doi:10.1016/j.gca.2003.09.012

Han, B. f., Ji, J. Q., and Song, B., (2006). Late paleozoic vertical growth of continental crust around the Junggar Basin, xinjiang, China (part: I): Timing of post-collisional plutonism. *Acta Pet. Sin.* 22 (5), 1077–1086.

Hao, F., Guo, T. L., Zhu, Y. M., Cai, X. Y., Zou, H. Y., and Li, P. P. (2008). Evidence for multiple stages of oil cracking and thermochemical sulfate reduction in the Puguang gas field, Sichuan Basin, China. *Am. Assoc. Pet. Geol. Bull.* 92 (5), 611–637. doi:10.1306/01210807090

Hay, R. L. (1966). Zeolites and zeolitic reactions in sedimentary rocks. *GSA Spec. Pap.* 85, 1–122. doi:10.1130/SPE85-p1

Himmler, T., Bach, W., Bohrmann, G., and Peckmann, J. (2010). Rare Earth elements in authigenic methane-seep carbonates as tracers for fluid composition during early diagenesis. *Chem. Geol.* 277 (1–2), 126–136. doi:10.1016/j.chemgeo.2010.07.015

Hu, W. X., Kang, X., Cao, J., Wang, X. L., Fu, B., and Wu, H. G. (2018). Thermochemical oxidation of methane induced by high-valence metal oxides in a sedimentary basin. *Nat. Commun.* 9 (5131), 1–10. doi:10.1038/s41467-018-07267-x

Huang, L., Liu, Y., Bian, B., Ma, Y., Liu, H., Guo, J., et al. (2021). Chemically active elements of reservoir quartz cement trace hydrocarbon migration in the Mahu Sag, Junggar Basin, NW China. *Geofluids* 2021, 6617945. doi:10.1155/2021/6617945

Irwin, H., Curtis, C., and Coleman, M. (1977). Isotopic evidence for source of diagenetic carbonates formed during burial of organic-rich sediments. *Nature* 269 (5625), 209–213. doi:10.1038/269209a0

Jin, Z. J., Zhang, L. P., Yang, L., and Hu, W. X. (2002). Primary study of geochemical features of deep fluids and their effectiveness on oil/gas reservoir formation in sedimental basins. *Earth Sci.* 27 (6), 659–665. Available at: http://www.earth-science.net/fileDQKX/journal/article/dqkxzx/2002/6/1182.pdf.

Kang, X., Hu, R. P., Hu, W. X., and Tan, J. Q. (2021). Oxidizing materials during thermochemical oxidation of hydrocarbons in the lower triassic Baikouquan Formation in the Junggar Basin. *Adv. Earth Sci.* 36 (10), 1004–1014. doi:10.11867/j.issn.1001-8166.2021.019

Kang, X., Hu, W., Cao, J., Wu, H., Xiang, B., and Wang, J. (2019). Controls on reservoir quality in fan-deltaic conglomerates: Insight from the lower triassic Baikouquan Formation, Junggar Basin, China. *Mar. Pet. Geol.* 103, 55–75. doi:10.1016/j.marpetgeo.2019.02.004

Krouse, H. R., Viau, C. A., Eliuk, L. S., Ueda, A., and Halas, S. (1988). Chemical and isotopic evidence of thermochemical sulphate reduction by light hydrocarbon gases in deep carbonate reservoirs. *Nature* 333 (6172), 415–419. doi:10.1038/333415a0

Kuang, Li. C., Zhi, D. M., et al. (2022). Hydrocarbon accumulation conditions and exploration directions of large-scale lithologic-stratigraphic oil and gas reservoirs in Upper Wuerhe Formation of Upper Permian in Junggar Basin. *Acta Pet. Sin.* 43 (3), 325–340. doi:10.7623/syxb202203001

Li, S. (2004). Basin geodynamics background of formation of huge petroleum systems. *Earth Sci.* 29 (5), 505–512. Available at: http://www.earth-science.net/fileDQKX/journal/article/dqkxzx/2004/5/1479.pdf.

Liang, Y. S., He, D. F., Zhen, Y., Zhang, L., and Tian, A. J. (2018). Tectono-stratigraphic sequence and basin evolution of shawan sag in the Junggar Basin. *Oil Gas. Geol.* 39 (5), 943–954. doi:10.11743/ogg20180509

Liu, Q., Peng, W., Meng, Q., Zhu, D., Jin, Z., and Wu, X. (2020). Fractionation of carbon and hydrogen isotopes of TSR-altered gas products under closed system pyrolysis. *Sci. Rep.* 10 (12921), 1–14. doi:10.1038/s41598-020-69580-0

Liu, Y., Hu, W., Cao, J., Wang, X., Zhu, F., Tang, Q., et al. (2019). Fluid–rock interaction and its effects on the upper triassic tight sandstones in the sichuan basin, China: Insights from petrographic and geochemical study of carbonate cements. *Sediment. Geol.* 383, 121–135. doi:10.1016/j.sedgeo.2019.01.012

Ma, Y. S., He, D. F., Cai, X. Y., and Liu, B. (2017). Distribution and fundamental science questions for petroleum geology of marine carbonate in China. *Acta Pet. Sin.* 33 (94), 1007–1020. Available at: http://html.rhhz.net/ysxb/20170401.htm.

Minor, E. C., Tennant, C. J., and Brown, E. T. (2019). A seasonal to interannual view of inorganic and organic carbon and pH in Western Lake Superior. *J. Geophys. Res. Biogeosci.* 124 (2), 405–419. doi:10.1029/2018JG004664

Pan, C., Wang, J., Yu, S., Wang, X., Xiang, B., Liao, J., et al. (2021). Oil origins, mixing and biodegradation in southwestern Junggar Basin, NW China. *J. Pet. Sci. Eng.* 196, 108017. doi:10.1016/j.petrol.2020.108017

Peters, K. E., Walters, C. C., and Moldowan, J. M. (2005). *The biomarker guide*. Cambridge, United Kingdom: Cambridge University Press.

Qiu, N. S., Yang, H. B., and Wang, X. L. (2002). Tectono-thermal evolution in the Junggar Basin. *Chin. J. Geol.* 37, 423–429. doi:10.3321/j.issn:0563-5020.2002.04.005

Sample, J. C., Torres, M. E., Fisher, A., Hong, W. L., Destrigneville, C., Defliese, W. F., et al. (2017). Geochemical constraints on the temperature and timing of carbonate formation and lithification in the Nankai Trough, NanTroSEIZE transect. *Geochim. Cosmochim. Acta* 198, 92–114. doi:10.1016/j.gca.2016.10.013

Seewald, J. S. (2001). Aqueous geochemistry of low molecular weight hydrocarbons at elevated temperatures and pressures: Constraints from mineral buffered laboratory experiments. *Geochim. Cosmochim. Acta* 65, 1641–1664. doi:10.1016/S0016-7037(01)00544-0

Seewald, J. S. (2003). Organic–inorganic interactions in petroleum-producing sedimentary basins. *Nature* 426 (6964), 327–333. doi:10.1038/nature02132

Shock, E. L. (1994). *Organic acids in geological processes*. Editors E. D. Pittman, and M. D. Lewan (New York: Springer), 270–318.

Spiro, B. (1977). Bacterial sulphate reduction and calcite precipitation in hypersaline deposition of bituminous shales. *Nature* 269 (5625), 235–237. doi:10.1038/269235a0

Sun, F., Hu, W., Wu, H., Fu, B., Wang, X., Tang, Y., et al. (2021). Two-stage mineral dissolution and precipitation related to organic matter degradation: Insights from *in situ* C-O isotopes of zoned carbonate cements. *Mar. Pet. Geol.* 124, 104812. doi:10.1016/j.marpetgeo.2020.104812

Surdam, R. C., Boese, S. W., and Crossey, L. J. (1984). The chemistry of secondary porosity: Part 2. Aspects of porosity modification. *AAPG Mem.* 37 (2), 127–161.

Surdam, R. C., Crossey, L. J., Hagen, E. S., and Heasler, H. P. (1989). Organic-inorganic interactions and sandstone diagenesis. *AAPG Bull.* 73 (1), 1–23.

Surdam, R. C., Jiao, Z. S., and MacGowan, D. B. (1993). Redox reactions involving hydrocarbons and mineral oxidants: A mechanism for significant porosity enhancement in sandstones. *Am. Assoc. Pet. Geol. Bull.* 77 (9), 1509–1518. doi:10.1306/BDFF8ED4-1718-11D7-8645000102C1865D

Swart, P. K. (2015). The geochemistry of carbonate diagenesis: The past, present and future. *Sedimentology* 62 (5), 1233–1304. doi:10.1111/sed.12205

Tang, G., Wang, Q., Wyman, D. A., Li, Z. X., Zhao, Z. H., Jia, X. H., et al. (2010). Ridge subduction and crustal growth in the central asian orogenic belt: Evidence from late carboniferous adakites and high-Mg diorites in the Western junggar region, northern xinjiang (west China). *Chem. Geol.* 277 (3–4), 281–300. doi:10.1016/j.chemgeo.2010.08.012

Tao, K., Cao, J., Hu, W., Zhi, D., Lei, D., Tang, Y., et al. (2021). Petroleum system for the continuous oil play in the lacustrine Lower Triassic, Junggar Basin, China. *Am. Assoc. Pet. Geol. Bull.* 105, 2349–2380. doi:10.1306/07022119211

Walkden, G. M., and Berry, J. R. (1984). Natural calcite in cathodoluminescence: Crystal growth during diagenesis. *Nature* 308 (5959), 525–527. doi:10.1038/308525a0

Wan, Y., Bourdet, J., Hu, W., Kang, X., Heath, C., Qiu, Y., et al. (2021). Experimental investigations on the thermochemical oxidation of n-alkane and alcohol compounds by MnO_2 and Fe_2O_3 at temperatures up to 325 °C. *Chem. Geol.* 559, 119982. doi:10.1016/j.chemgeo.2020.119982

Wang, Y. S. (2016). "The features of fluid inclusions and their contained information on hydrocarbon migration and accumulation among permian systems in Zhongguai area, northwestern Junggar Basin," (Xi'an, China: Northwest University), 47–60. Unpubl. Master Thesis.

Wu, H., Hu, W., Tang, Y., Cao, J., Wang, X., Wang, Y., et al. (2017). The impact of organic fluids on the carbon isotopic compositions of carbonate-rich reservoirs: Case study of the lucaogou Formation in the jimusaer sag, Junggar Basin, NW China. *Mar. Pet. Geol.* 85, 136–150. doi:10.1016/j.marpetgeo.2017.05.003

Xi, K., Cao, Y., Jahren, J., Zhu, R., Bjørlykke, K., Haile, B. G., et al. (2015). Diagenesis and reservoir quality of the lower cretaceous quantou formation tight sandstones in the southern songliao basin, China. *Sediment. Geol.* 330, 90–107. doi:10.1016/j.sedgeo.2015.10.007

Xia, L., Cao, J., Bian, L., Hu, W., Wang, T., Zhi, D., et al. (2022). Co-evolution of paleo-environment and bio-precursors in a Permian alkaline lake, Mahu mega-oil province, Junggar Basin: Implications for oil sources. *Sci. China Earth Sci.* 65 (3), 462–476. doi:10.1007/s11430-021-9861-4

Xie, D., Yao, S., Cao, J., Hu, W., and Qin, Y. (2020). Origin of calcite cements and their impact on reservoir heterogeneity in the triassic yanchang formation, ordos basin, China: A combined petrological and geochemical study. *Mar. Pet. Geol.* 117, 104376. doi:10.1016/j.marpetgeo.2020.104376

Xie, X. N., Cheng, J. M., and Meng, Y. L. (2009). Basin fluid flow and associated diagenetic processes. *Acta Sediment. Sin.* 27 (5), 863–871. doi:10.14027/j.cnki.cjxb.2009.05.016

Yuan, G., Cao, Y., Qiu, L., and Chen, Z. (2017). Genetic mechanism of high-quality reservoirs in Permian tight fan delta conglomerates at the northwestern margin of the Junggar Basin, northwestern China. *Am. Assoc. Pet. Geol. Bull.* 101 (12), 1995–2019. doi:10.1306/02071715214

Zhang, C. J., He, D. F., Wu, X. Z., Shi, X., and Luo, J. (2006). Formation and evolution of multicycle superimposed basins in Junggar Basin. *China Pet. explor.* 1, 47–58. doi:10.3969/j.issn.1672-7703.2006.01.008

Zhang, G. C., Chen, X. F., Liu, L., Yu, L. P., and Wang, Z. (1999). The tectonic evolution, architecture and petroleum distribution in the Junggar Basin in China. *Acta Pet. Sin.* 20 (1), 13–18. Available at: https://www.cnki.com.cn/Article/CJFDTOTAL-SYXB901.002.htm.

Zhang, L. F., Lei, D. W., and Tang, Y., (2015). Hydrocarbon fluid phase in the deep-buried strata of the MaHu sag in the Junggar Basin. *Acta Geol. Sin.* 89 (5), 957–969. Available at: http://www.geojournals.cn/dzxb/ch/reader/create_pdf.aspx?file_no=2014195&st=alljournals.

Zhao, M. Y., Zheng, Y. F., and Zhao, Y. Y. (2016). Seeking a geochemical identifier for authigenic carbonate. *Nat. Commun.* 7 (1), 10885–10887. doi:10.1038/ncomms10885

Zhao, Z. H. (1997). *Principles of trace element geochemistry*. Bei Jing: Science Press.

Zhi, D. M., Kang, X., Qin, Z. J., Tang, Y., Cao, J., and Hu, R. P. (2022). Fluid-rock interactions and porosity Genesis in deep clastic reservoirs: A perspective of differential oil charge intensity. *Mar. Pet. Geol.* 137, 105508. doi:10.1016/j.marpetgeo.2021.105508

Zhu, G. Y., Zhang, S. C., Liang, Y. b., Ma, Y. S., Dai, J. X., and Zhou, G. Y. (2006). Dissolution and alteration of the deep carbonate reservoirs by TSR: An important type of deep-buried high-quality carbonate reservoirs in sichuan basin. *Acta Pet. Sin.* 22 (8), 2182–2194. doi:10.3969/j.issn.1000-0569.2006.08.008

Zhu, S. F., Zhu, X. M., Wang, X. L., and Liu, Z. Y. (2012). Zeolite diagenesis and its control on petroleum reservoir quality of Permian in northwestern margin of Junggar Basin, China. *Sci. China Earth Sci.* 55 (3), 386–396. doi:10.1007/s11430-011-4314-y

Zou, C. N., Hou, L. H., Kuang, L. C., and Kuang, J. (2007). Genetic mechanism of diagenesis-reservoir facies of the fan-controlled Permo-Triassic in the Western marginal area, Junggar Basin. *China J. Geol.* 42 (3), 587–601. doi:10.1016/S1872-5791(07)60044-X